Word count 6127

Strain-induced partial serpentinization of germanate olivine with a small amount of water

Sando Sawa[1], Nobuyoshi Miyajima[2], Jun Muto[1], Hiroyuki Nagahama[1]

1. Department of Earth Science, Tohoku University, Sendai 980-8578, Japan

2. Bayerisches Geoinstitut, University of Bayreuth, Bayreuth 95440, Germany

Abstract

Antigorite, a high-pressure polymorph of serpentine, is considered to be the most abundant hydrous mineral in the subduction zone. Although the antigorite is presumed as one of the origins of intermediate-depth earthquakes in the subduction zone, the amount of antigorite is uncertain because the amount of water infiltrated into the oceanic lithosphere is still debated. To investigate whether antigorite can be formed even under the limited availability of water, we conducted the axial deformation experiments of magnesium germanate at 1.2 GPa and T = 500-800 °C using a Griggs-type deformation apparatus. Magnesium germanate is an analog material of magnesium silicate, and the absorbed water in the starting material was eliminated preliminary. Nevertheless, the samples had initially high porosity, and hence the small amount of water (about 200 ppm wt H_2O) was retained in

the samples. In the samples deformed at 600 ℃, the stable slip occurred, and TEM analysis revealed that fine-grained platelets of germanate antigorite existed along the faults. Sharp absorption band assigned to the OH stretching vibration of antigorite in Fourier transform infrared spectroscopic (FT-IR) analysis also implies that antigorite widely was formed in the samples deformed at temperature lower than 600 ℃. Our results indicate that strain-induced hydration of germanate olivine results in antigorite formation even under a small amount of water. Thus, partly hydrated peridotite in the oceanic lithosphere can be formed under slight water infiltration due to high strain accumulated by the subduction.

Introduction

Olivine, $(Mg, Fe)_2SiO_4$, and its high-pressure polymorphs are the most abundant minerals in the upper mantle (Irifune and Ringwood 1987). Therefore, these magnesium silicates play an important role in the mantle rheology. However, deformation experiments under the stability field of high-pressure polymorphs of magnesium silicates are difficult to be conducted until recently (Kawazoe et al. 2016). Because olivine phase of magnesium germanate can undergo the phase transformation to the spinel phase at lower pressures than that of magnesium silicate (Ross and Navrotsky 1987), magnesium germanate has been used

2

as an analog material of the magnesium silicate (e.g., Vaughan and Coe 1981; Green and Burnley 1989; Schubnel et al. 2013; Shi et al. 2015; Wang et al. 2017).

Olivine also undergoes a metamorphic transformation to serpentine minerals (lizardite, chrysotile, and antigorite) by a hydration reaction. Serpentine minerals contain 12.3 wt% water and are a great career of water into the interior of the Earth (e.g., Evans et al. 2013). In particular, antigorite, a high-temperature polymorph of serpentine, is the most common hydrous mineral under the condition of 300-650 °C up to 6 GPa covering a wide range of the subduction zone (Hacker et al. 2003). Antigorite has different physicochemical and rheological properties from olivine, so it has a strong influence on deformation partitioning and seismicity in the subduction zone (e.g., Hirauchi et al. 2010). The faulting associated with the dehydration of antigorite has also been considered as a candidate to explain the intermediate-depth earthquakes (e.g., Raleigh and Paterson 1965; Hacker et al. 2003; Yamasaki and Seno 2003; Ferrand et al. 2017).

Large and deep normal faulting at the outer-rise after a megathrust earthquake could enhance the infiltration of fluids into the deep lithospheric mantle (e.g., Obana et al. 2012). Therefore, the peridotite in the oceanic lithosphere is considered to be hydrated (serpentinized) adequately (e.g., Ranero et al. 2003). Meanwhile, elevated pressures prevent

3

water infiltration along the faults (Korenaga 2017). Hence, the amount of antigorite is predicted to be small as deeper (Shillington et al. 2015; Korenaga 2017) or little (Reynard et al. 2010). Therefore, it is important to investigate whether antigorite can be formed even under the limited availability of water in the oceanic lithosphere.

Although many previous studies of serpentinization have been conducted as hydrothermal experiments which are under excess water for serpentinization (e.g., Martin and Fyfe 1970; Okamoto et al. 2011; Oyanagi et al. 2017) and a large amount of water (Malvoisin et al. 2012; Nakatani and Nakamura 2019), no experiments have been done under the small amount of water. Furthermore, magnesium germanate has many studies about the olivine and spinel phase, but germanate serpentine was only reported by Roy and Roy (1954), Nesterchuk et al. (1984), and Ropp (2013). In this study, in order to reveal the formation of germanate serpentine under the small amount of water, we firstly eliminated excess water in the magnesium germanate sample by heating and then conducted deformation experiments of the sample with a small amount of water. By microstructural observation of the recovered samples, we revealed whether antigorite could be formed even under the small amount of water by strain enhanced hydration reaction.

4

Experimental procedure

Sample preparation

The samples used in this study were synthesized germanate olivine-pyroxene aggregates (90 mol% Mg_2GeO_4 + 10 mol% $MgGeO_3$). Germanate aggregates were synthesized from a powder mixture of MgO and GeO_2 according to Vaughan and Coe (1981) and Shi et al. (2015). Stoichiometric powders of MgO and GeO_2 with 2 : 1.05 molar ratios were made by grinding the powders together with ethanol in an agate mortar. Then the powders were pressed into the cylindrical shape in stainless steel dies. The cold-pressed specimens were heated in air at 1200 ℃ for 96 h. Cylindrical samples with a height of 10 mm and a diameter of 6.25 mm were cored from the aggregates. The porosity is calculated to be about 28±3 % by its volume, weight, and density but decreases to 16 % from the result of volume decrease of the sample in experiment GO137, which was stopped just before deformation at 600 ℃ and 1.2 GPa. XRD analysis of samples clarified that the powders contained neither MgO nor GeO_2. Electron backscatter diffraction (EBSD, Oxford instruments) clarified the presence of no initial crystallographic orientation and mean grain size less than 10 μm (shown in Figure S1). These samples were heated at 900 ℃ and 1 hour to eliminate excess water. However, Fourier transform infrared spectroscopy (FT-IR)

5

clarified that they show a weak absorption band around 2800-3700 cm^{-1} derived from molecular water containing about 196±8.4 wt ppm H_2O initially (shown later for the calculation details) based on Bolfan-Casanova et al. (2014).

Deformation experiments

Axial deformation experiments were performed in a Griggs-type deformation apparatus installed in Tohoku University, Japan. The procedure of the deformation experiments was based on Kido et al. (2016). The construction of the assembly is following to Chernak et al. (2009), Kido et al. (2016), and Fukuda et al. (2018). The schematic diagram of the whole assembly is shown in Figure 1. Sample assembly made of talc and NaCl as an outer and an inner pressure media, respectively, was used for the deformation experiments. However, NaCl was used as an outer pressure medium only in GO134. The cored samples were cut into two short cores perpendicular to their longitudinal direction, and a Ni strain marker was placed between the cores. The samples were heated at 900 °C for 1 hour before the deformation experiments. Then, they were packed into a metal jacket using metal discs at each end. Ag was used as the material at the experimental temperatures of 500 and 600 °C, meanwhile, Pt was used for 700 and 800 °C. Then, they were slid into an outer Ni jacket that

6

slightly overlapped the end pistons. Table 1The temperature was measured using an S-type

thermocouple. The temperature and pressure were raised as follows: from room temperature

to 100 ℃ at 300 MPa, to 200 ℃ at 550 MPa, and 300 ℃ at 1050 MPa to stay within the

stability field of liquid water in the sample. The deformation piston was advanced until the

piston touches the top of the sample associated with a dramatic increase in the axial stress,

known as a hit point (Holyoke and Kronenberg 2010). At this time, Pb, as a weak solid to

seal the upper portion of the assembly between the sample and alumina pistons, is squeezed

out along the deformation piston. Then, the piston is backed off 0.5 mm above the hit point.

Pressure and temperature were elevated by the confining pressure of 1.2 GPa and the target

temperatures, and an axial compression experiment was immediately performed with a

constant strain rate of 2.0×10^{-4} s^{-1}. All experiments were performed within the stability field

of germanate spinel phase (Ross and Navrotsky 1987), but germanate olivine retained

metastable state before the onset of axial compression experiments because the rate of

temperature increases from 300 ℃ to the target temperature is fast (within 1 h). At the end

of each experiment, the temperature decreased to room temperature within 1 min, and the

deformation was stopped. The force and displacement data were converted to differential

stress and strain values, respectively, with corrections for changes in the sample diameter and

7

the apparatus distortion. The stress resolution of the Griggs-type apparatus has been estimated to be ±30 MPa (Holyoke and Kronenberg 2010; Kido et al. 2016). We also conducted an experiment to check the microstructural development and the initial sample porosity just before the deformation experiment (GO137). The experimental conditions are listed in Table 1.

Microstructural observation

All deformed and starting samples were cut into halves along the direction parallel to axial stress and impregnated with epoxy to analyze the microstructures. Samples were polished with diamond paste and colloidal silica and observed by a field emission scanning electron microscope (SEM, JEOL 7001F) in Tohoku University, Japan.

Sample GO126 was also observed with a transmission electron microscope (TEM, Philips CM20FEG, and FEI Titan G2 80-200 S/TEM) in University of Bayreuth, Germany with an accelerating voltage of 200.0 kV. For TEM analysis, we made a TEM foil from a thin section of GO126 with a dual-beam focused ion beam milling machine (FIB, FEI Scios, BGI).

Water contents of the starting and all deformed samples were measured using a FT-IR micro-spectrometer (Nicolet iS10, Thermo Scientific) in Tohoku University, Japan. The

8

measurements were taken with a rectangular aperture of 100×100 μm^2. IR spectra were

obtained by averaging 100 scans. In the starting material, the spectra were integrated from

3700 to 2800 cm^{-1}. Meanwhile, in GO124, GO125, and GO126, a peak separation of the

spectra was performed, and the OH absorption peaks were integrated only around 3630

cm^{-1} to eliminate the spectra of epoxy. We used the Beer-Lambert law to calculate the water

contents

$$C = \frac{AX}{\varepsilon t},$$

where C is the water concentration (ppm wt H$_2$O), A is the integrated absorbance, X is

the density factor (L mol H$_2$O^{-1}), ε is the absorption coefficient (L mol H$_2$O^{-1} cm^{-2}) and t

is the sample thickness (cm). $X = 18.10 \times 10^3/\rho$, where ρ is the density of the phase

(g/cm^3) (Bolfan-Casanova et al. 2014). In this study, we adopt the density of germanate

olivine $\rho = 3.97$ g/cm^3 (Liebermann 1975). $\varepsilon = 246.6(3753 - v)$, where v is the mean

weavnumber (Libowitzky and Rossman 1997). Water contents of the starting material and

deformed samples are averaged over randomly selected two and six locations, respectively.

To determine the mineral phases in all samples, we analyzed these sections with

9

micro-Raman spectroscopy (JASCO NRS-4100TOR) in Tohoku University. Observed

Raman bands were assigned according to Guyot et al. (1986).

Results

Mechanical data

The stress-strain curves of deformation experiments were shown in Figure 2.

Stress-strain curves of axial deformation experiments. In the sample GO124 deformed at the

lowest temperature (500 ℃), stress increases rapidly and never reached yielding. The

samples GO126 (600 ℃) and GO134 (700 ℃) show rapid strain weakening behaviors after

the peak differential stresses around 1 ~ 1.5 GPa. Then, the sample GO134 reaches steady-

state behavior after further strain (>30% strain). The sample GO125 deformed at the highest

temperature (800 ℃) is weaker than others and showed steady-state behavior soon after small

amount of strain (< 5% strain).

The maximum unloading slopes during strain weakening behaviors in samples

GO126 and GO134 are 2.4 GPa/mm and 1.4 GPa/mm, respectively, and are less than the

effective unloading stiffness of the apparatus ~ 8.8 GPa/mm reported in the previous study

(Chernak and Hirth 2011).

10

Microstructure

Raman spectroscopy clarified that aggregates in GO124, GO126, and GO134 were composed of olivine (α-Mg$_2$GeO$_4$) and orthopyroxene, but those in GO125 were completely transformed into germanate cubic spinel (γ-Mg$_2$GeO$_4$) and clinopyroxene after experiments.

Figure 3a and b show back-scattered electron (BSE) images of sample GO126. Fig. 3a shows a large fault oriented to the 30° with respect to the σ_1 direction (whole image of the sample is shown in Figure S2). A Ni strain marker is split into two parts by the fault with a clear offset of about 200 μm. Figure 3b shows a part of the fault gouge in a conjugate relation to the main fault in Figure 3a (white dashed lines in Figure S2). The conjugate fault is oriented 30° with respect to the σ_1 direction and composed of fine-grained materials. A FIB foil was extracted from the fault (red rectangle in Fig. 3b).

Figure 3c shows the whole BSE image of GO134. The large fault divides the sample into two halves. Although the large offset and subsequent deformation inhibit the precise estimate of the fault displacement, a conservative estimate is more than 2.0 mm.

Figure 4 shows TEM images of the fault in the FIB foil extracted from GO126 (red rectangle in Figure 3b). The fault composed of fine-grained aggregates runs from the upper

11

left to the bottom right in Figure 4a. The detailed microstructure of the fault is shown in Figure 4b and c. In the fault zone, grains shown by red arrows are sharply sheared with grain comminution down to 50 nm (Figure 4b). Figure 4c shows large olivine grains along the fault. We observed many small platelets surrounding large olivine grains (red arrows). The width of the platelets is about 30 nm. Although the accurate estimate is not possible, the length is at least 100 nm. A selected area electron diffraction (SAED) pattern of an olivine grain including surrounding platelets in the central part of Figure 4c is shown in Figure 4d. The strong diffraction spots are derived from germanate olivine grains. In addition, weak diffraction spots with a d-spacing of 0.74 nm that cannot be indexed either by germanate olivine (d-spacing ~ 0.515 nm, Robbins and Levin 1959), spinel (d-spacing ~ 0.476 nm, Von Dreele et al. 1977), or pyroxene (d-spacing ~ 0.646 nm, Robbins and Levin 1959) were observed, but the d-spacing fits to that of antigorite. Furthermore, they show topotactic relationships between the (100) of germanate olivine and the (001) of the platelets (Figure S4).

Water content

Figure 5 shows the results of FT-IR measurements of the starting material and all

12

deformed samples. Although FT-IR measurements were conducted at various locations in each sample, there were no clear differences at locations except sharp peaks around 3650 cm^{-1} in GO125 (see also Fig. S3 and discussed later in this chapter). A broad absorption peak from 2800 to 3700 cm^{-1} is assigned to molecular water (Aines and Rossman 1984; Keppler and Rauch 2000). Therefore, the broad absorption peak from 2800 to 3700 cm^{-1} in the starting material indicates the presence of the absorbed water. The absorption peaks from 2800 to 3000 cm^{-1} are unique to alkane or alkene which is likely originated from epoxy (Socrates 2004). Samples GO124 and GO126 also show a similar sharp absorption band at 3630 cm^{-1}. Because of the characteristic OH-band of silicate antigorite around 3630 cm^{-1} (Heller-Kallai et al. 1975), the peak is assigned to an OH-band of germanate antigorite.

Several spectra of sample GO125 only show a dominant peak at 3630 cm^{-1} similar to OH-band assigned to germanate antigorite (Figure S3). On the other hand, a rather wide absorption band at 3650 cm^{-1} in GO125 with a shoulder at 3688 cm^{-1} (shown by red arrows in Figure S3) can be assigned to the OH-band originated from germanate spinel phase (Thomas et al. 2008).

Table 1 summarizes the water content of samples GO124, GO125, and GO126 calculated by the integration around 3630 cm^{-1} derived from OH-band of germanate

13

antigorite.

Discussion

Formation and a stable slip of antigorite

TEM analysis of the germanate olivine aggregates deformed under high pressure and temperature revealed small platelets were formed along the fault in germanate olivine aggregates (Fig. 4c). They were topotactically grew to the surrounding olivine (Fig. 4d) and indexed neither by olivine nor pyroxene. TEM analysis of partially serpentinized natural olivine originated from the Oman ophiolite (Boudier et al. 2010) and the subcontinental mantle of the Adriatic lithosphere (Morales et al. 2018) shows similar topotactic relationships between antigorite and olivine: $(001)_{atg}//(100)_{ol}$ (Boudier et al. 2010; Morales et al. 2018). Furthermore, the (001) plane of germanate antigorite has a d-spacing of 0.7474 nm (Nesterchuk et al. 1984). Therefore, the d-spacing of 0.74 nm of small platelets observed in this study is a characteristic for the (001) plane of the germanate antigorite structure. Although starting materials were heated before experiments to eliminate the absorbed water in the fine-grained porous aggregates (initial average porosity of about 28 %), a small amount of water should remain in the aggregates. Furthermore, the presence of the sharp absorption

14

peak at 3630 cm^{-1} assigned to an OH-band of antigorite implies that germanate antigorite was formed by the reaction to absorbed water with germanate olivine during deformation. In particular, the initial porosity of GO124 is higher than others, so that the amount of absorbed water in the sample is likely to be large. Although TEM analysis on the limited area found the antigorite platelets only around the fault zone, the presence of FTIR absorption peaks at 3630 cm^{-1} observed in randomly selected locations in samples GO124 and GO126 indicates that germanate antigorite could widely exist in samples.

Formation of small platelets of germanate antigorite along the fault zone likely controls the rheological behaviors of the sample GO126. Proctor and Hirth (2016) conducted the shear deformation experiments of silicate antigorite serpentine gouges at temperatures of 300-500 °C and pressures of 1-2 GPa and revealed the inverse ductile to brittle transition with increasing temperature. With an increase in temperature, the coefficient of friction decreases, and strain was observed to be localized on faults developed in the gouges (Proctor and Hirth 2016). The coefficient of friction is related to the ratio of the shear strength of asperity contacts to the indentation hardness of the asperities (Hirth and Guillot 2013; Scholz 2019). If antigorite slip surfaces are oriented parallel to its basal plane, asperity contacts can be easily sheared because the basal plane is an easy glide plane. The increasing temperature

15

would reduce the shear stress compared with the penetration hardness by enhancing dislocation glide thus reducing the coefficient of friction (Hirth and Guillot 2013; Proctor and Hirth 2016). Although the amount of antigorite is observed to be quite low in GO126 by TEM, the sharp peak in FTIR spectra at 3630 cm^{-1} implies the ubiquitous presence of antigorite in the samples, and antigorite would exist widely along the fault. Hence, the presence of germanate antigorite at 600 °C would result in strain localization and faulting (frictional sliding) accompanying a clear weakening. The existence of the absorption peak near 3630 cm^{-1} in GO124 implies that further strain likely results in a similar weakening behavior in the sample, whereas it was difficult to confirm whether the slip occurs in the sample because the axial stress of about 4.0 GPa was close to the limit of this apparatus. Although we also observed clear faulting with strain weakening in GO134, the reason for the faulting is uncertain. The fault plane was oriented high angle with respect to the compression direction, so faulting could occur along the weak Ni strain marker by heterogeneous deformation due to high initial sample porosity.

Because the unloading slope during faulting (GO126: 2.4 GPa/mm and GO134: 1.4 GPa/mm) was less than the effective unloading stiffness of the apparatus 8.8 GPa/mm, those slip events in germanate antigorite were stable sliding in this study. This is consistent with

16

the results of the shear experiments of silicate antigorite serpentine (Moore and Lockner 2007; Takahashi et al. 2011; Hirauchi et al. 2016). In contrast to both experiments conducted at low pressure under water-saturated (Moore and Lockner 2007) and the controlled pore pressure (Takahashi et al. 2011) conditions, this study had no pore pressure, but the stable slip would occur due to hydration reaction being consistent with the previous study conducted at high pressure (Hirauchi et al. 2016). Green and Burnley (1989) and Burnley et al. (1991) also conducted the deformation experiments of magnesium germanate at similar pressures (1-3 GPa) and temperatures from 600 to 1200 °C. The partial phase transformation from the olivine to the spinel phase resulted in faulting with a large stress drop ($\Delta\sigma \sim 900$ MPa). The phase transformation is a thermally activated process so that the faulting and unstable slip were observed at the limited condition of temperature (800-1000 °C). At lower temperatures (< 800 °C), the samples showed ductile behavior with a maximum differential stress > 2.0 GPa (called strong ductile behavior). Meanwhile, at the higher temperature (> 1000 °C), the samples showed ductile behavior with a maximum differential stress < 1.0 GPa (called weak ductile behavior) because the olivine phase underwent the phase transformation to the spinel phase completely. The mechanical data for the sample GO125 with complete phase transformation in this study also indicate the weak ductile behavior (steady-state flow

17

behavior at maximum differential stress < 0.5 GPa). Unlike previous studies showing the

unstable slip due to the partial phase transformation to spinel, the sample in this study showed

the stable slip due to the partial serpentinization. This is likely caused by the difference in the

porosity and absorbed water resulting in the stable slip due to antigorite formation.

Implications for the mechanism of serpentinization in the oceanic lithosphere

The amount of antigorite in the oceanic lithosphere remains enigmatic because water

infiltration required to form antigorite becomes more difficult as deeper due to elevated

pressure (Korenaga 2017). However, the infiltration of water into the oceanic lithosphere

could be promoted along a large and deep outer-rise normal fault (e.g., Ranero et al. 2003;

Obana et al. 2012). Stress changes induced by the bending oceanic plate produce negative

pressure gradients along the fault favoring downward pumping of water, and hence enhance

the infiltration of water (Faccenda et al. 2009). Fault damages along the normal fault could

lead to the hydration in the deep part of the oceanic lithosphere (Iyer et al. 2012). Based on

effects of serpentinization and crack porosity on the seismic velocities, the degree of

serpentinization at the upper 10 km of the oceanic lithosphere is estimated to be 10 %

corresponding to 1.2 wt% H_2O (Lefeldt et al. 2012). Korenaga (2007, 2017) also pointed out

18

that even small crack-like porosities (0.1-0.2 %) pre-existed in the oceanic lithosphere

produced by thermal cracking also causes hydration of the oceanic lithosphere reaching 300-

700 ppm wt% H_2O (seawater or serpentinite) at the lower Wadati-Benioff seismic plane.

Eventually, the oceanic lithosphere is considered to be partly hydrated (> 300 ppm wt% H_2O)

along these faults or cracks.

In this study, the initial porosity (16 %) was much higher than that estimated in the

oceanic lithosphere (at least 0.1-0.2 %), and the amount of water left in samples (about 200

ppm wt% H_2O) is slightly smaller than the minimum value (~300 ppm wt% H_2O). However,

we observed the germanate antigorite in the deformed samples. This implies that antigorite

may be formed in the oceanic lithosphere with the small amount of water. As Korenaga

(2017) pointed out, porosity in the oceanic lithosphere can be locally higher than this value.

Ruptures associated with a large and deep outer-rise normal fault may cause transient

porosity along fault and cracks in the upper or middle part of the oceanic lithosphere. Hence

a small amount of water can be easily incorporated into the oceanic lithosphere. Furthermore,

brittle faulting increases the surface area of grains, so hydration reaction can be enhanced by

the brittle faulting. As a mechanism of serpentinization in such oceanic lithosphere with only

small amount of water and locally high porosity, this study proposes a possibility that even a

19

small amount of water can form antigorite under high strain (shear-enhanced partial

serpentinization) because the ocean lithosphere can accumulate high strain during subduction.

Funding

Acknowledgements

References

Aines, R.D., and Rossman, G.R. (1984) Water in minerals? A peak in the infrared. Journal of Geophysical Research: Solid Earth, 89, 4059–4071.

Bolfan-Casanova, N., Montagnac, G., and Reynard, B. (2014) Measurement of water contents in olivine using Raman spectroscopy. American Mineralogist, 99, 149–156.

Boudier, F., Baronnet, A., and Mainprice, D. (2010) Serpentine mineral replacements of natural olivine and their seismic implications: oceanic lizardite versus subduction-related antigorite. Journal of Petrology, 51, 495–512.

Burnley, P.C., Green, H.W., and Prior, D.J. (1991) Faulting associated with the olivine to spinel transformation in Mg_2GeO_4 and its implications for deep-focus earthquakes. Journal of Geophysical Research, 96, 425-443.

Chernak, L.J., and Hirth, G. (2011) Syndeformational antigorite dehydration produces stable fault slip. Geology, 39, 847–850.

Chernak, L.J., Hirth, G., Seiverstone, J., and Tullis, J. (2009) Effect of aqueous and carbonic fluids on the dislocation creep strength of quartz. Journal of Geophysical Research: Solid Earth, 114, 1–18.

21

Evans, B.W., Hattori, K., and Baronnet, A. (2013) Serpentinite: What, why, where? Elements, 9, 99–106.

Faccenda, M., Gerya, T. V., and Burlini, L. (2009) Deep slab hydration induced by bending-related variations in tectonic pressure. Nature Geoscience, 2, 790–793.

Ferrand, T.P., Hilairet, N., Incel, S., Deldicque, D., Labrousse, L., Gasc, J., Renner, J., Wang, Y., Green, H.W., and Schubnel, A. (2017) Dehydration-driven stress transfer triggers intermediate-depth earthquakes. Nature Communications, 8, 1–11.

Fukuda, J., Muto, J., and Nagahama, H. (2018) Strain localization and fabric development in polycrystalline anorthite + melt by water diffusion in an axial deformation experiment. Earth, Planets and Space, 70, 3.

Green II, H.W., and Burnley, P.C. (1989) A new self-organizing mechanism for deep-focus earthquakes. Nature, 341, 733–737.

Guyot, F., Boyer, H., Madon, M., Velde, B., and Poirier, J.P. (1986) Comparison of the raman microprobe spectra of $(Mg, Fe)_2SiO_4$ and Mg_2GeO_4 with olivine and spinel structures. Physics and Chemistry of Minerals, 13, 91–95.

Hacker, B.R., Peacock, S.M., Abers, G.A., and Holloway, S.D. (2003) Subduction factory 2. Are intermediate-depth earthquakes in subducting slabs linked to metamorphic

dehydration reactions? Journal of Geophysical Research: Solid Earth, 108, 2030.

Heller-Kallai, L., Yariv, S., and Gross, S. (1975) Hydroxyl-stretching frequencies of

serpentine minerals. Mineralogical Magazine, 40, 197–200.

Hirauchi, K., Michibayashi, K., Ueda, H., and Katayama, I. (2010) Spatial variations in

antigorite fabric across a serpentinite subduction channel: Insights from the Ohmachi

Seamount, Izu-Bonin frontal arc. Earth and Planetary Science Letters, 299, 196–206.

Hirauchi, K., Fukushima, K., Kido, M., Muto, J., and Okamoto, A. (2016) Reaction-

induced rheological weakening enables oceanic plate subduction. Nature

Communications, 7, 12550.

Hirth, G., and Guillot, S. (2013) Rheology and tectonic significance of serpentinite.

Elements, 9, 107–113.

Holyoke, C.W., and Kronenberg, A.K. (2010) Accurate differential stress measurement

using the molten salt cell and solid salt assemblies in the Griggs apparatus with

applications to strength, piezometers and rheology. Tectonophysics, 494, 17–31.

Irifune, T., and Ringwood, A.E. (1987) Phase transformations in a harzburgite composition

to 26 GPa: implications for dynamical behaviour of the subducting slab. Earth and

Planetary Science Letters, 86, 365–376.

23

Iyer, K., Rüpke, L.H., Morgan, J.P., and Grevemeyer, I. (2012) Controls of faulting and

reaction kinetics on serpentinization and double Benioff zones. Geochemistry,

Geophysics, Geosystems, 13, 1–18.

Kawazoe, T., Nishihara, Y., Ohuchi, T., Miyajima, N., Maruyama, G., Higo, Y., Funakoshi,

K. ichi, and Irifune, T. (2016) Creep strength of ringwoodite measured at pressure–

temperature conditions of the lower part of the mantle transition zone using a

deformation–DIA apparatus. Earth and Planetary Science Letters, 454, 10–19.

Keppler, H., and Rauch, M. (2000) Water solubility in nominally anhydrous minerals

measured by FTIR and ^{1}H MAS NMR: The effect of sample preparation. Physics and

Chemistry of Minerals, 27, 371–376.

Kido, M., Muto, J., and Nagahama, H. (2016) Method for correction of differential stress

calculations from experiments using the solid salt assembly in a Griggs-type

deformation apparatus. Tectonophysics, 672–673, 170–176.

Korenaga, J. (2007) Thermal cracking and the deep hydration of oceanic lithosphere: A key

to the generation of plate tectonics? Journal of Geophysical Research: Solid Earth,

112, 1–20.

——— (2017) On the extent of mantle hydration caused by plate bending. Earth and

24

Planetary Science Letters, 457, 1–9.

Lefeldt, M., Ranero, C.R., and Grevemeyer, I. (2012) Seismic evidence of tectonic control

on the depth of water influx into incoming oceanic plates at subduction trenches.

Geochemistry, Geophysics, Geosystems, 13.

Libowitzky, E., and Rossman, G.R. (1997) An IR absorption calibration for water in

minerals. American Mineralogist, 82, 1111–1115.

Liebermann, R.C. (1975) Elasticity of olivine (α), beta (β), and spinel (γ) polymorphs of

germanates and silicates. Geophysical Journal of the Royal Astronomical Society, 42,

899–929.

Malvoisin, B., Brunet, F., Carlut, J., Rouméjon, S., and Cannat, M. (2012) Serpentinization

of oceanic peridotites: 2. Kinetics and processes of San Carlos olivine hydrothermal

alteration. Journal of Geophysical Research: Solid Earth, 117.

Martin, B., and Fyfe, W.S. (1970) Some experimental and theoretical observations on the

kinetics of hydration reactions with particular reference to serpentinization. Chemical

Geology, 6, 185–202.

Moore, D.E., and Lockner, D.A. (2007) Comparative deformation behavior of minerals in

serpentinized ultramafic rock: Application to the slab-mantle interface in subduction

zones. International Geology Review, 49, 401–415.

Morales, L.F.G., Mainprice, D., and Kern, H. (2018) Olivine-antigorite orientation

relationships: Microstructures, phase boundary misorientations and the effect of cracks

in the seismic properties of serpentinites. Tectonophysics, 724–725, 93–115.

Nakatani, T., and Nakamura, M. (2019) Preferential orthopyroxene serpentinization and

implications for seismic velocity interpretation in the fore-arc mantle. Journal of

Geophysical Research: Solid Earth, 124, 3420–3435.

Nesterchuk, N.I., Makarova, T.A., Romanov, D.P., and Grebenshchikov, R.G. (1984)

Synthesis and properties of manganese and magnesium hydrogermanate. Bulletin of

the Academy of Sciences of the USSR Division of Chemical Science, 33, 1717–1719.

Obana, K., Fujie, G., Takahashi, T., Yamamoto, Y., Nakamura, Y., Kodaira, S., Takahashi,

N., Kaneda, Y., and Shinohara, M. (2012) Normal-faulting earthquakes beneath the

outer slope of the Japan Trench after the 2011 Tohoku earthquake: Implications for the

stress regime in the incoming Pacific plate. Geophysical Research Letters, 39, 1–7.

Okamoto, A., Ogasawara, Y., Ogawa, Y., and Tsuchiya, N. (2011) Progress of hydration

reactions in olivine–H_2O and orthopyroxenite–H_2O systems at 250 °C and vapor-

saturated pressure. Chemical Geology, 289, 245–255.

26

Oyanagi, R., Okamoto, A., and Tsuchiya, N. (2017) Mechanisms of serpentinization utilizing olivine–plagioclase–H_2O System under hydrothermal conditions. Procedia Earth and Planetary Science, 17, 686–689.

Proctor, B., and Hirth, G. (2016) "Ductile to brittle" transition in thermally stable antigorite gouge at mantle pressures. Journal of Geophysical Research: Solid Earth, 121, 1652–1663.

Raleigh, C.B., and Paterson, M.S. (1965) Experimental deformation of serpentinite and its tectonic implications. Journal of Geophysical Research, 70, 3965-3985.

Ranero, C.R., Morgan, J.P., McIntosh, K.D., and Reichert, C. (2003) Flexural faulting and mantle serpentinization at the Middle American. Nature, 425, 367–373.

Reynard, B., Nakajima, J., and Kawakatsu, H. (2010) Earthquakes and plastic deformation of anhydrous slab mantle in double Wadati-Benioff zones. Geophysical Research Letters, 37, 1–6.

Robbins, C.R., and Levin, E.M. (1959) The system magnesium oxide-germanium dioxide. American Journal of Science, 257 (1), 63-70.

Ropp, R.C. (2013) Encyclopedia of the Alkaline Earth Compounds, 1–1187 p. Elsevier.

Ross, N.L., and Navrotsky, A. (1987) The Mg_2GeO_4 olivine-spinel phase-transition.

27

Physics and Chemistry of Minerals, 14, 473–481.

Roy, D.M., and Roy, R. (1954) An experimental study of the formation and properties of

synthetic serpentines and related layer silicate minerals. American Mineralogist, 39,

957–975.

Scholz, C.H. (2019) The Mechanics of Earthquakes and Faulting. Cambridge University

Press.

Schubnel, A., Brunet, F., Hilairet, N., Gasc, J., Wang, Y., and Green, H.W. (2013) Deep-

focus earthquake analogs recorded at high pressure and temperature in the laboratory.

Science, 341, 1377–1380.

Shi, F., Zhang, J., Xia, G., Jin, Z., and Green, H.W. (2015) Rheology of Mg_2GeO_4 olivine

and spinel harzburgite: Implications for Earth's mantle transition zone. Geophysical

Research Letters, 42, 2212–2218.

Shillington, D.J., Becel, A., Nedimovic, M.R., Kuehn, H., Webb, S.C., Abers, G.A.,

Keranen, K.M., Li, J., Delescluse, M., and Mattei-Salicrup, G.A. (2015) Link between

plate fabric, hydration and subduction zone seismicity in Alaska. Nature Geoscience,

8, 961–964.

Socrates, G. (2004) Infrared and Raman characteristic group frequencies: tables and charts,

366 p. John Wiley & Sons, Ltd.

Takahashi, M., Uehara, S.I., Mizoguchi, K., Shimizu, I., Okazaki, K., and Masuda, K.
(2011) On the transient response of serpentine (antigorite) gouge to stepwise changes
in slip velocity under high-temperature conditions. Journal of Geophysical Research:
Solid Earth, 116.

Thomas, S.M., Koch-Müller, M., Kahlenberg, V., Thomas, R., Rhede, D., Wirth, R., and
Wunder, B. (2008) Protonation in germanium equivalents of ringwoodite, anhydrous
phase B, and superhydrous phase B. American Mineralogist, 93, 1282–1294.

Vaughan, P.J., and Coe, R.S. (1981) Creep mechanism in Mg_2GeO_4: Effect of a phase
transition. Journal of Geophysical Research, 86, 389–404.

Von Dreele, R.B., Navrotsky, A., and Bowman, A.L. (1977) Refinement of the crystal
structure of Mg_2GeO_4 spinel. Acta Crystallographica Section B Structural
Crystallography and Crystal Chemistry, 33, 2287–2288.

Wang, Y., Zhu, L., Shi, F., Schubnel, A., Hilairet, N., Yu, T., Rivers, M., Gasc, J., Addad,
A., Deldicque, D., and others (2017) A laboratory nanoseismological study on deep-
focus earthquake micromechanics. Science Advances, 3, e1601896.

Yamasaki, T., and Seno, T. (2003) Double seismic zone and dehydration embrittlement of

29

the subducting slab. Journal of Geophysical Research: Solid Earth, 108, 1–21.
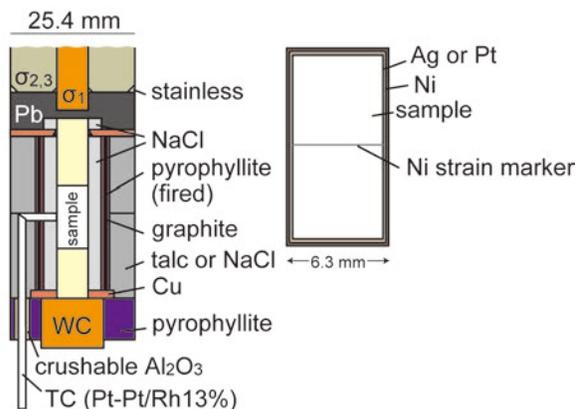
Figure 1

Figure 1. Schematic diagram of the whole sample assembly (left) and inner sample assembly modified

after Fukuda et al. (2018).

Table 1. Experimental conditions and results conducted at a pressure of 1.2 GPa and various temperatures.

Experimental No.	T (°C)	σ (MPa)	ε (%)	Phase	H_2O content (wt ppm H_2O)
GO124	500	1570	24	Olivine	399±13
GO125	800	380	42	Spinel	127±17
GO126	600	1810	31	Olivine	177±11
GO134	700	1330	38	Olivine	-
GO137	600[a]	-	-	-	-

Notes: T: temperature, *σ*: peak differential stress and *ε*: axial strain.

a: This temperature was estimated from the power-temperature relations of previous experiments.
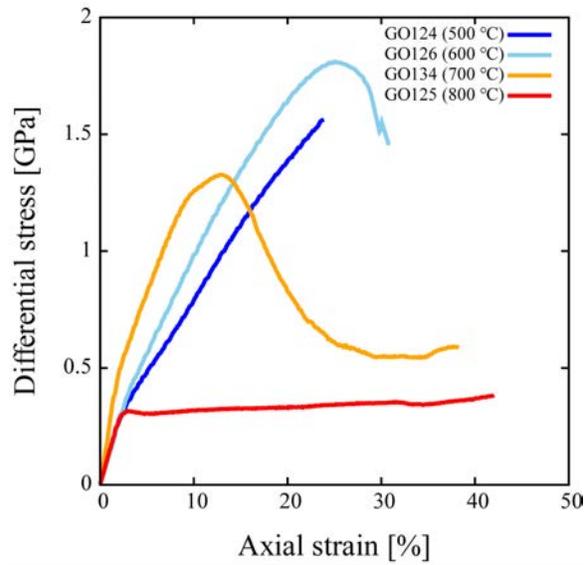
Figure 2

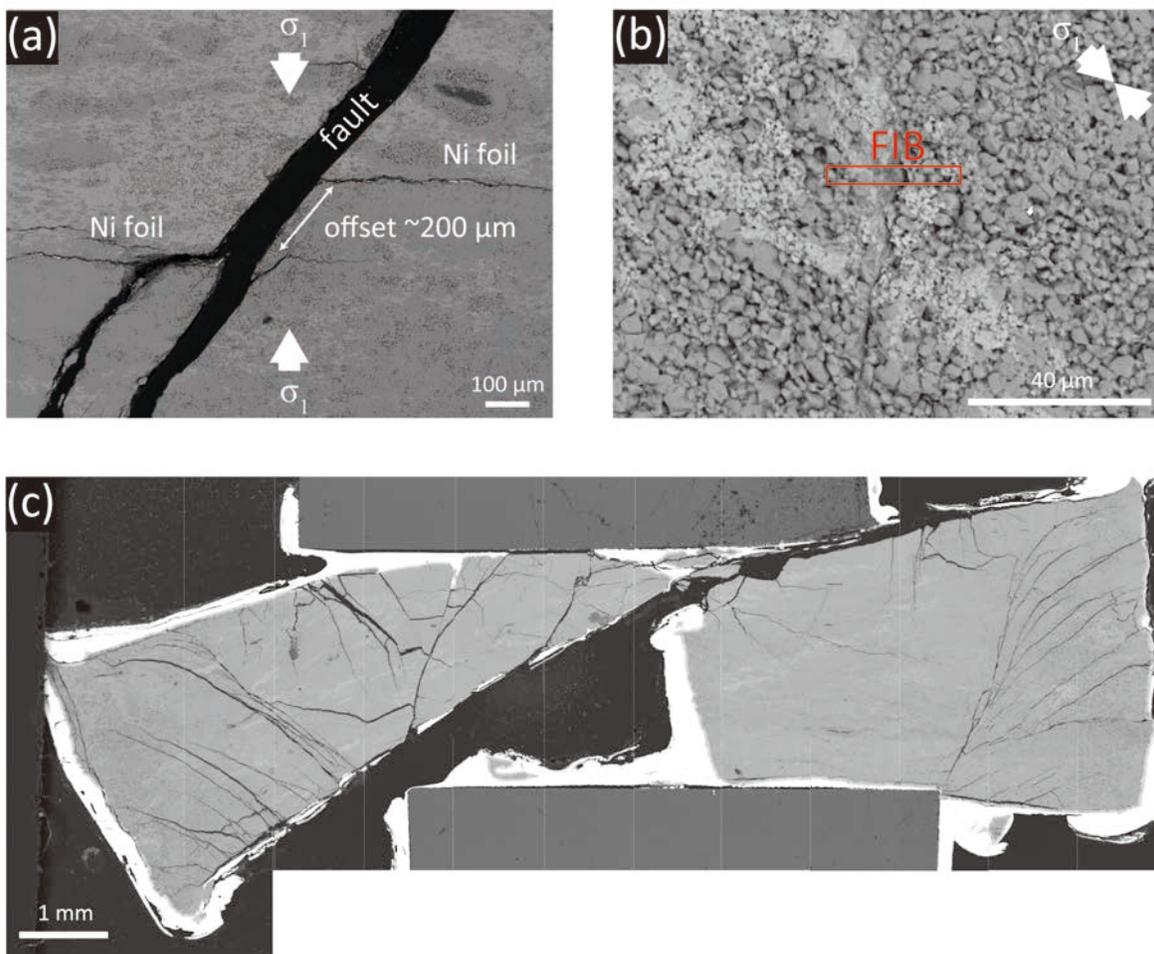**Figure 2.** Stress-strain curves of axial deformation experiments.

Figure 3

Figure 3. Back-scattered electron (BSE) images of GO126 (a,b) and GO134 (c). The gray minerals are germanate olivine, and the light gray minerals are germanate pyroxene. (a): The large fault divides a piece of Ni foil into two parts. The fault offset is about 200 μm. (b): The FIB foil was made at the red rectangle in the fault gouge. (c): The whole image of GO134. The large fault divides the whole sample into two halves.
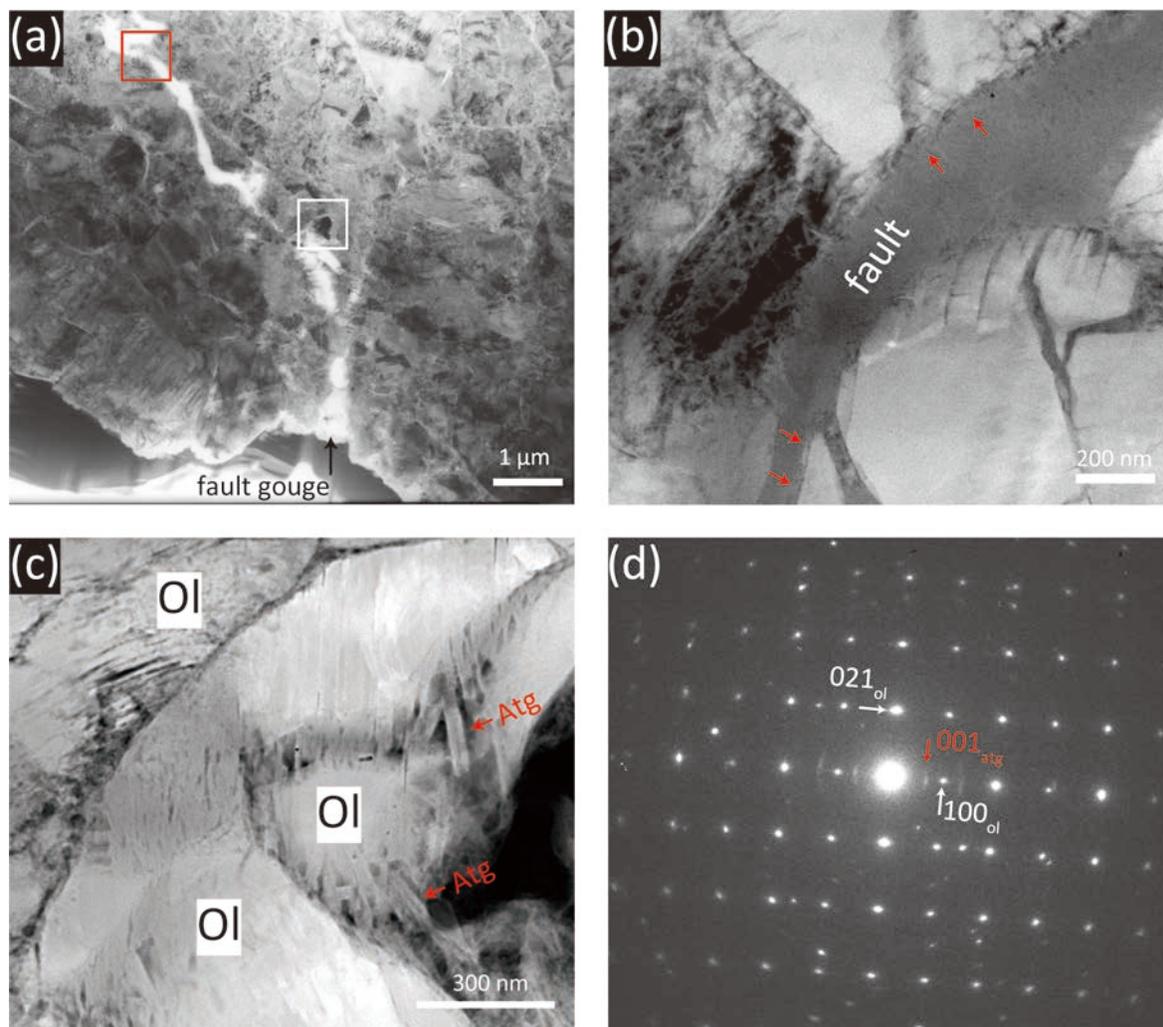
33

Figure 4

Figure 4. TEM images of GO126 in a FIB foil extracted from the red rectangle in Figure 3c: (a) bright-field TEM image, (b, c) high-angle annular dark-field (HAADF) scanning TEM images and (d) the selected area electron diffraction (SAED) pattern corresponding to the center part of (c). (a): White fissure from the upper left to the bottom is fault gouge. The detailed microstructure along the fault is shown in (b) and (c). (b): The fault corresponding to the red box in (a). Grains are sheared by the fault (red arrows).

(c): Olivine grains along the fault corresponding to the white box in (a). Many small platelets of germanate

antigorite (red arrows) can be seen near white-colored germanate grains. (d): The SAED pattern shows

topotactic relations between the germanate antigorite (atg) platelets and the parent germanate olivine (ol)
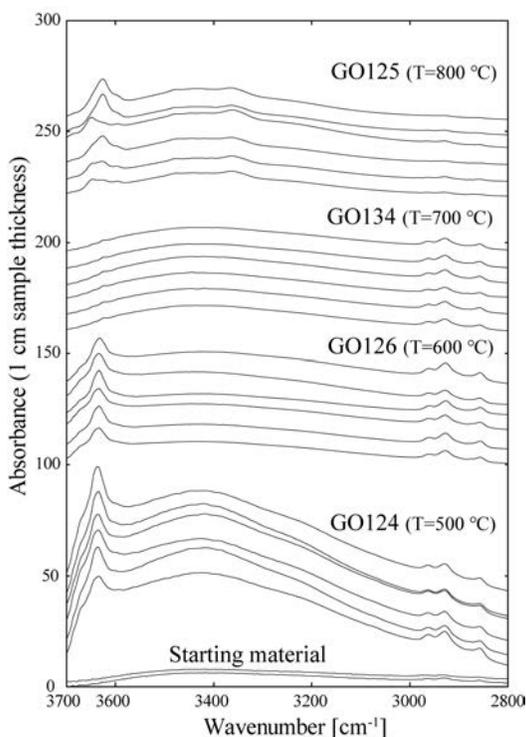
grain.

Figure 5

Figure 5. The infrared absorption spectra of the starting material and deformed samples. Broad absorption

bands centered at 3400 cm^{-1} are derived from molecular water such as absorbed water and epoxy.

Absorption peaks from 2800 to 3000 cm^{-1} are originated from epoxy. An absorption peak near 3630 cm^{-1}

in GO124 and GO126 is derived from an OH-band of antigorite, whereas the absorption peak near 3630

cm^{-1} in GO125 is derived from an OH-band of germanate antigorite or germanate spinel.